# 6. ANTARCTICA

## a. Overview—S. Stammerjohn and T. Scambos

Last year we reported on Antarctic climate anomaly patterns in 2015 that produced strong positive southern annular mode (SAM) index values which persisted until austral spring. Climate patterns then distinctly shifted and the anomalies intensified in response to the 2015 El Niño (Stammerjohn 2016). In 2016, Antarctic climate anomalies were again aligned with strong positive SAM index values, particularly for the first third of the year. By austral spring 2016, however, anomaly patterns reversed, leading to strong negative SAM index values. The pressure anomalies (negative SAM index) persisted and strengthened during October to December, such that Antarctic-wide climate anomalies stood in stark contrast not only to 2016's beginning, but also to the previous several years. Additional highlights for 2016:

- March and June set new monthly high SAM index values (since 1957) of +4.36 and +3.66, respectively. Monthly low pressure records for March, June, and September were also broken at many stations. During this time, overall sea ice extent and area were close to the 1981–2010 average.

- With low surface temperatures prevailing during the 2015/16 melt season (generally November–February), most of the continent and ice shelves showed negative melt duration anomalies (compared to 1981–2010). However, the Ross Ice Shelf showed an unusual and widespread positive melt season relative to the 1981–2010 mean. Although the Antarctic Peninsula (AP) typically experiences the longest melt seasons relative to the rest of the continent, the AP melt duration anomalies in 2015/16 were mostly negative.

- Climate patterns flipped in October–December, with high surface pressure over the continent, weaker westerly winds, and higher surface temperatures prevailing, leading to negative SAM index values, with a sharp intensification in November. Monthly high pressure records for August and November were set at several stations. During this period, record low daily and monthly sea ice extents were observed.

The November mean sea ice extent was over 5 standard deviations below the 1981–2010 average. These record low sea ice values in austral spring 2016 contrast sharply with the record high values observed during 2012–14.

- Upper ocean positive thermal anomalies in the austral summer–fall of 2016 were tightly coupled to subsequent austral winter sea ice anomalies, suggesting some preconditioning by the ocean. Conversely, austral spring–summer sea ice anomalies in 2015/16 were spatially consistent with upper ocean salinity anomalies in the subsequent austral summer–fall, suggesting that net spring sea ice melt was a strong influence on upper ocean salinity.

- An open-ocean polynya was observed over Maud Rise in winter 2016. Although modest in size compared to its appearances in 1974–76, the 2016 polynya is significant as it may announce a revival of deep ocean convection in the eastern Weddell Sea.

- Assessments of deep ocean observations support the hypothesis that increased input of freshwater from the ice sheet and changes in sea ice transport continue to contribute to observed Southern Ocean deepwater freshening. A sidebar highlights two new ocean observing programs aimed at improving our understanding of the Southern Ocean's role in capturing anthropogenic carbon and heat.

- Over the last 18 years, the austral spring ozone hole has displayed some indications of diminishing, and 2016 was no exception, with a slightly less severe ozone hole than in earlier decades.
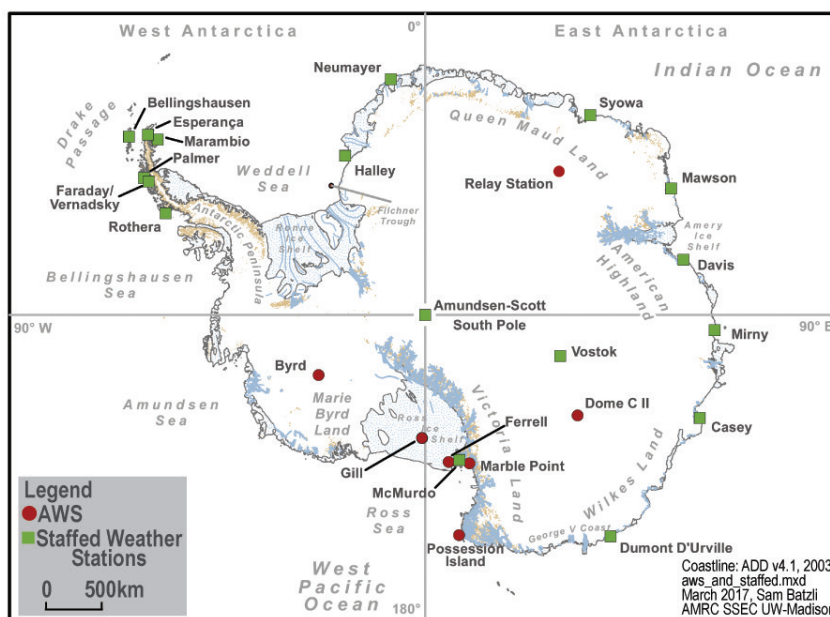


FIG. 6.1. Map of stations and other regions discussed in the chapter.

Details on the state of Antarctica's climate in 2016 are provided below, beginning with the atmospheric circulation, surface observations, sea ice, and ocean observations, and ending with the Antarctic ozone hole. Place names used throughout this chapter are provided in Fig. 6.1.

### b. Atmospheric circulation—K. R. Clem, S. Barreira, and R. L. Fogt

Antarctica experienced persistent below-average pressures and surface temperatures at the beginning of 2016, which led to positive SAM index values through April. Marshall (2003) describes the SAM and the basis for the index. In brief, the SAM index indicates the strength of the annular pressure and wind pattern surrounding the southern continent. It is determined by the difference in the zonally averaged mean sea level pressures at 40°S and 65°S. The 2016 austral winter and spring had record positive SAM indices, but with larger month-to-month variability. Between June and September, the continent had lower-than-average temperatures, except for the month of August, which had warmer-than-average conditions. At the end of the year, strong positive pressure and surface temperature anomalies occurred over the continent, producing negative SAM index values for October to December.

A closer look at the Antarctic circulation and temperature anomalies is given in Figs. 6.2 and 6.3. Figure 6.2 shows the geopotential height and temperature anomalies averaged over the polar region (the "polar cap": all areas south of 60°S; Figs. 6.2a and b, respectively) and the circumpolar zonal wind anomalies averaged over 50° to 70°S from ERA-Interim reanalysis (Fig. 6.2c). Anomalies are contoured and the standard deviations are shaded. Given the large month-to-month variability in winter, the year is split into six periods of relatively persistent climatic features: January–April, May–June, July, August, September,

and October–December. The groups are indicated by vertical red bars at the bottom of each panel in Fig. 6.2. Surface anomalies for the six groups are shown in Fig. 6.3, with the standardized surface pressure anomalies contoured and standardized 2-meter temperature anomalies shaded. In all cases, anomalies and standard deviations are with respect to the 1981–2010 climatological mean.
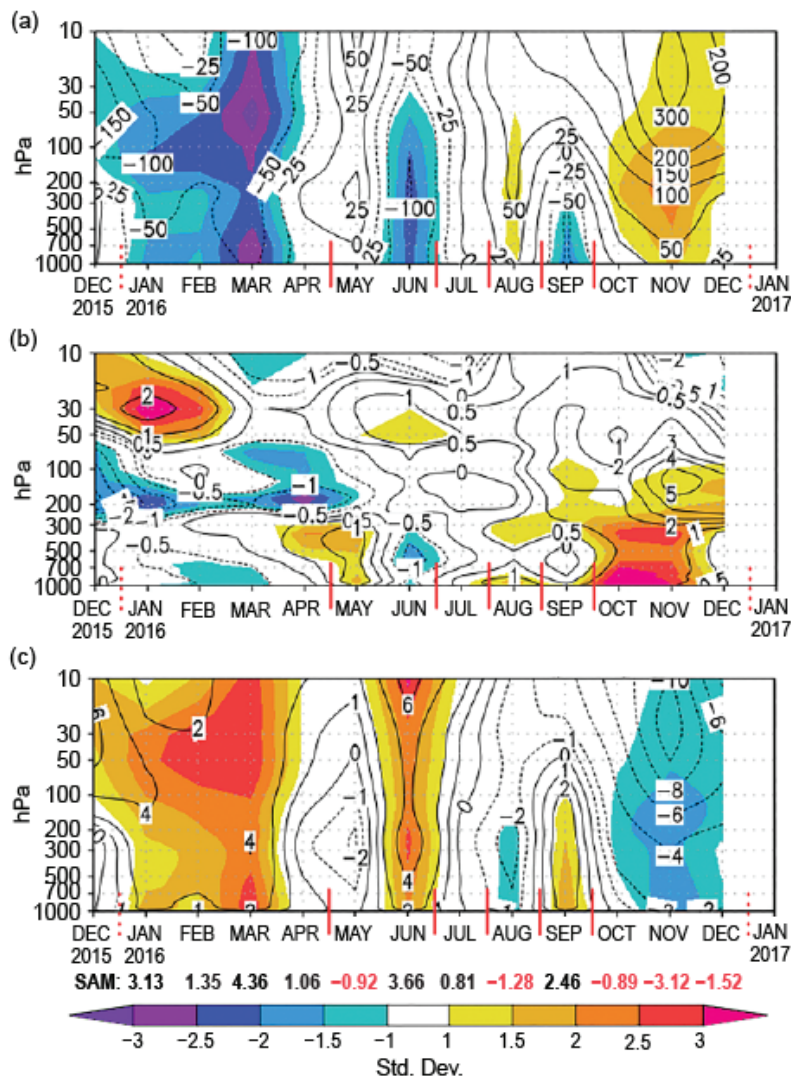


**FIG. 6.2. Area-averaged (weighted by cosine of latitude) anomalies over the southern polar region in 2016 relative to 1981–2010: (a) polar cap (60°–90°S) averaged geopotential height anomalies (contour interval is 50 m up to ± 200 m with additional contour at ± 25 m, and 100 m contour interval after ± 200 m); (b) polar cap averaged temperature anomalies (contour interval is 1°C with additional contour at ± 0.5°C); (c) circumpolar (50°–70°S) averaged zonal wind anomalies (contour interval is 2 m s⁻¹ with additional contour at ± 1 m s⁻¹). Shading represents std. dev. of anomalies. Red vertical bars indicate the six climate periods used for compositing in Fig. 6.3; the dashed lines near Dec 2015 and Dec 2016 indicate circulation anomalies wrapping around the calendar year. Values from the Marshall (2003) SAM index are shown below (c): positive (black) and negative (red). (Source: ERA-Interim reanalysis.)**
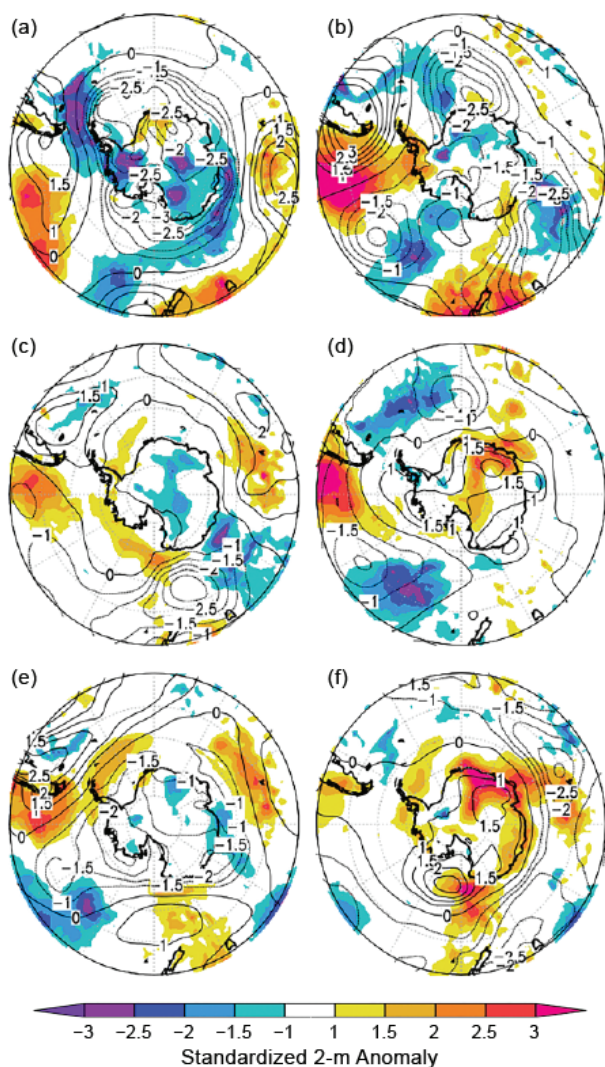
**FIG. 6.3.** Standardized surface pressure (contours) and 2-m temperature (shaded) anomalies relative to 1981–2010 for (a) Jan–Apr 2016; (b) May–Jun 2016; (c) Jul 2016; (d) Aug 2016; (e) Sep 2016; (f) Oct–Dec 2016. Contour interval is 0.5 std. dev. of surface pressure anomalies with the ±0.5 contour omitted. Shading represents std. dev. of 2-m temperature anomalies. (Source: ERA-Interim reanalysis.)

During January–April, negative geopotential height (Fig. 6.2a) and surface pressure (Fig. 6.3a) anomalies were observed over Antarctica, with negative surface temperature anomalies everywhere across the continent except Queen Maud Land. Strong positive circumpolar zonal wind anomalies of 2–4 m s$^{-1}$ (>2 standard deviations above the climatological mean) were observed through the troposphere and stratosphere (Fig. 6.2c), and the SAM index set a monthly record-high value (since 1957) of +4.36 in March and reaching its third highest monthly value on record for January (+3.13; based on the Marshall index and archive). The circulation pattern weakened

during May, characterized by weak positive height and temperature anomalies over the polar cap but transitioned back to a strong positive SAM index during June, setting another monthly record-high SAM value of +3.66. Despite the strong positive SAM index value during June, the May–June average circulation consisted of a zonal wave three pattern with three anomalous troughs located along ~55°S near 0°, 135°E, and 135°W (Fig. 6.3b). The wave three pattern was associated with above-average sea ice concentration in the eastern Weddell Sea, Davis Sea, and western Amundsen Sea during May–June (see Section 6f). Above-average surface temperature anomalies occurred across the Antarctic Peninsula during May–June while the remainder of the continent was near-average to slightly colder than average. Aloft, strong negative geopotential height and temperature anomalies occurred through the troposphere over the polar cap during June, and positive circumpolar zonal wind anomalies were seen through the troposphere and stratosphere. These exceeded 2 standard deviations above the climatological average, reflecting the strong positive SAM index in June.

The circulation edged closer to its climatological mean over the continent during July (Fig. 6.3c), with near-average temperatures and pressure/heights across the polar cap (except for weak positive surface temperature anomalies over the West Antarctic coast and weak negative surface temperature anomalies over portions of interior East Antarctica) and an average strength of the circumpolar westerlies. During August (Fig. 6.3d), positive surface pressure and temperature anomalies were seen across most of the continent, except for some weak surface cooling along the Antarctic Peninsula. The surface warming during August was strongest over eastern East Antarctica across Queen Maud Land and Enderby Land where positive temperature anomalies of 3°–6°C (not shown) were observed, exceeding 2.5 standard deviations above the climatological mean. The circulation switched back to a zonal wave three and positive SAM index pattern for September, with three anomalous ridges (>1 standard deviation) located along ~55°S at 75°E, 180°, and 60°W (orange-red shaded areas in Fig. 6.3e). Much of Antarctica saw near-average to slightly-below-average surface temperatures during September except for the Antarctic Peninsula, which was 3°–5°C warmer than average (not shown) and exceeded 1.5 standard deviations above the climatological mean (orange-red shading in Fig. 6.3e). The positive SAM index value of +2.46 for September tied 1959 as the fourth highest value on record for the month.

Strong positive pressure anomalies developed over Antarctica from October to November as positive geopotential height anomalies propagated downward from the stratosphere into the lower troposphere, maximizing in November (Fig. 6.2a). The anomalous high pressure over the polar cap resulted in a strong weakening of the circumpolar westerlies (Fig. 6.2c) and widespread surface warming along coastal Antarctica and over portions of interior Antarctica (Fig. 6.3f), leading to rapid sea ice retreat in many regions (see Section 6f). The surface warming was again strongest across western Queen Maud Land and Enderby Land, where October–December surface temperatures were 2°–3°C above average (not shown) and 3 standard deviations above the climatological mean (orange-red shading in Fig. 6.3f). Strong surface warming was also found across the Antarctic Peninsula and Marie Byrd Land, both of which were warmer than average and 1–1.5 standard deviations above the climatological mean. The SAM index was negative for all three months to close 2016, reaching a maximum negative value of −3.12 during November, which was the fifth lowest SAM index value on record for that month; this corresponded to a period of rapid sea ice loss after the maximum extent in September 2016 (see Section 6f).

*c. Surface observations*—L. M. Keller, S. Colwell, M. A. Lazzara, and R. L. Fogt

Monthly mean temperatures on the Antarctic Peninsula were generally above the long-term (1981–2010) means for the entire year. Late May experienced some very warm conditions (Fig. 6.3b) with Rothera Station recording a daily maximum temperature of 7.5°C on 26 May, and 11.2°C on 30 May at Marambio Station.

In the Weddell Sea and Queen Maud Land regions, monthly mean temperatures at Halley Station were close to the long-term average, with the exception of June (Fig. 6.4b). The average June monthly temperature was −34.2°C, 2.2°C below the previous coldest value. At Neumayer Station, a record high monthly mean temperature for May of −15.5°C was followed by a record low monthly mean temperature of −28.7°C in June. The monthly temperature then remained above the long-term mean at Neumayer for the rest of the year. Very low pressures (8–11 hPa below normal) were recorded in March and May at Neumayer, and March and June at Halley, reflecting the strongly positive SAM index conditions.

Around the coast of East Antarctica, all of the Australian stations and Syowa Station reported new record high monthly mean temperatures in November (Casey: −3.7°C; Davis: −2.2°C; Mawson: −2.8°C;

Syowa: −4.7°C; Figs. 6.3f, 6.4c), and Syowa Station also had record high monthly mean temperatures in August and October (−13.9°C and −9.3°C, respectively; Figs. 6.3d, 6.3f). Pressures at Syowa, Mawson, and Davis stations were below average for most of the year with above-average values recorded in August, November, and December. Farther around the East Antarctic coast, record-breaking low monthly mean pressures were recorded at Casey (Fig. 6.4c) and Dumont D'Urville stations for March (966.8 hPa and 972.4 hPa), June (972.2 hPa, 975.9 hPa), and September (964.4 hPa, 969.5 hPa), respectively.

At Amundsen–Scott Station (Fig. 6.4a) and Vostok Station, the monthly mean temperatures were close to the long-term means with the exception of July (lower) and August (higher) at Amundsen–Scott and June (lower), July (lower) and August (higher) at Vostok Station. Record-breaking low monthly mean surface pressures were recorded at both Amundsen–Scott and Vostok in June (672.1 and 613.0 hPa, respectively), and a record-breaking high monthly mean pressure was recorded at Vostok Station in November (635.0 hPa).

From the automatic weather stations (AWS), the western side of Antarctica reported lower-than-normal mean monthly temperatures for the first half of the year. Ferrell AWS had lower-than-normal mean temperatures for April, June, and July (approximately 3°–4°C below average), while Byrd AWS (Fig. 6.4e) observed below-normal mean temperatures for February, March, June, and September (2°–4°C below average). Above-average mean temperatures were reported at Byrd for July, August, and October (by +2°–3°C). Gill AWS (Fig. 6.4f), in the middle of the Ross Ice Shelf (see Fig. 6.1), had lower-than-normal mean temperatures for June and July (−3° to −5°C), but a record high monthly mean temperature was set in January (−5.5°C), and a higher-than-normal temperature was reported in August. In East Antarctica, Marble Point AWS reported conditions similar to Ferrell; Dome C II reported lower-than-average mean temperatures for March and April (about 2°–3°C lower) and a record high monthly mean temperature in November (−34.2°C). Relay AWS (Fig. 6.4d) observed lower-than-average mean temperatures for June and July (−5.3° and −2.3°C, respectively) and higher-than-average temperatures for October and November (about 5°C above normal). Record high monthly mean temperatures were set in March (−5.8°C) and August (−5.6°C).

Along with lower temperatures for the first part of the year in West Antarctica, most of the AWSs reported lower-than-average mean monthly station pressures generally through June with many low pres-
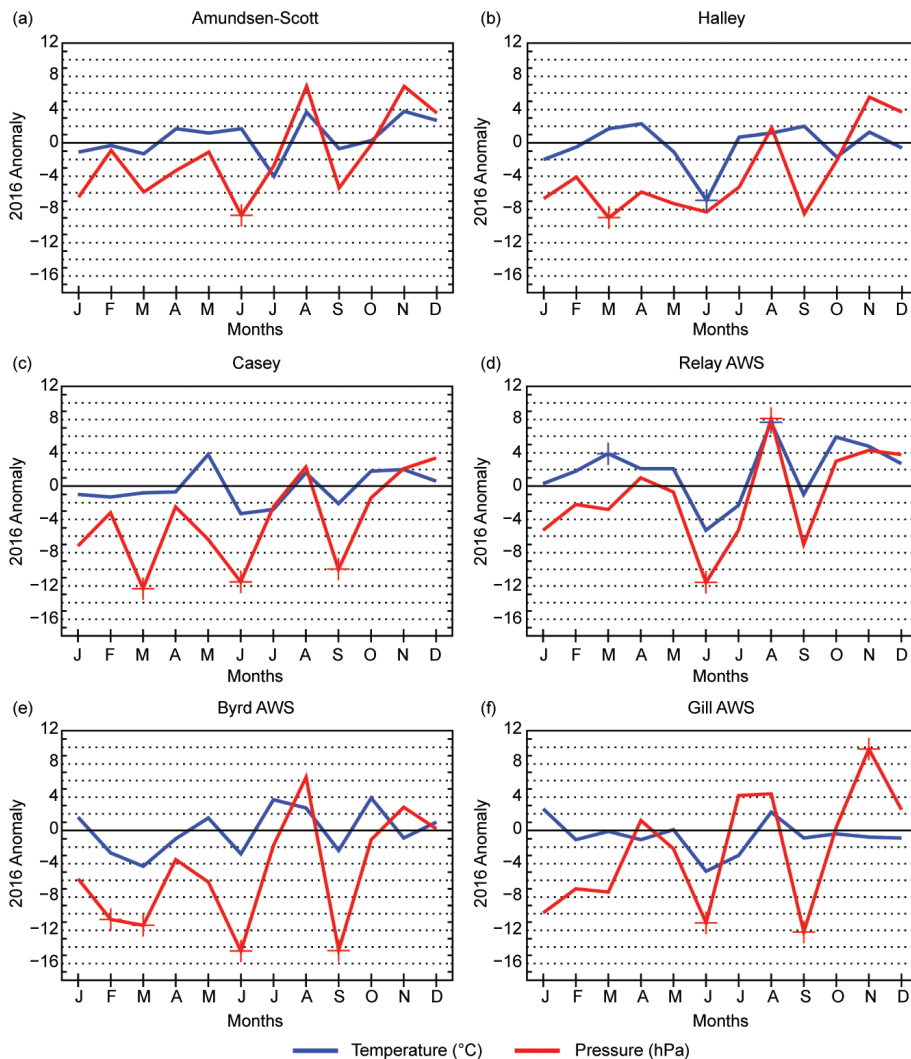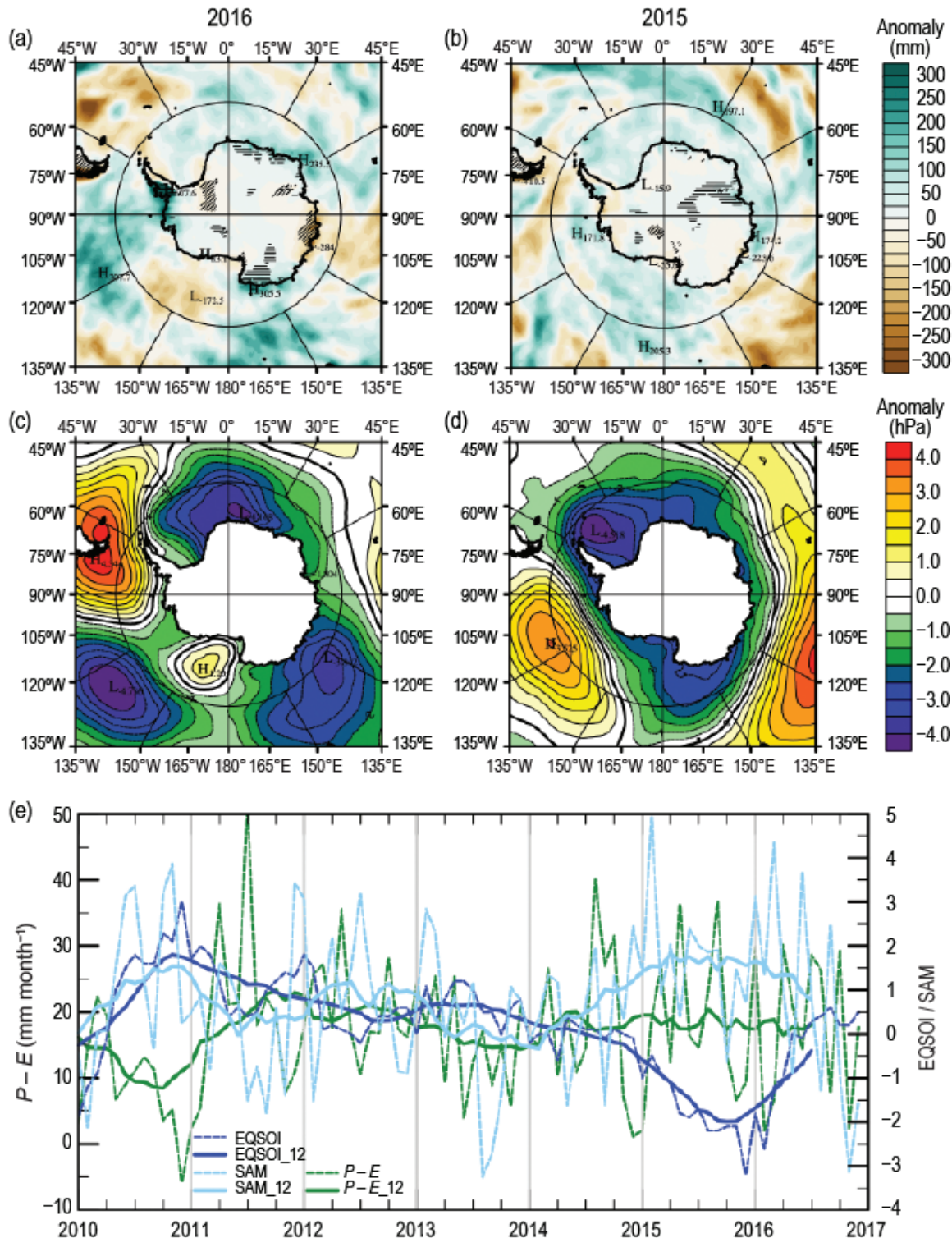
**Fig. 6.4. 2016 Antarctic climate anomalies at six representative stations [three staffed (a)–(c), and three automatic (d)–(f)]. Monthly mean anomalies for temperature (°C) in blue and MSLP/surface pressure (hPa) in red are shown, with + denoting record anomalies for a given month at each station in 2016. All anomalies are based on differences from 1981–2010 averages, except for Gill, which is based on averages during 1985–2015. Observational data start in 1957 for Amundsen–Scott and Halley, 1959 for Casey, 1995 for Relay AWS, 1981 for Byrd AWS, and 1985 for Gill AWS. See Turner et al. (2004) and Lazzara et al. (2012) for details on the station and AWS data.**

plateau station Dome C II also reported lower than normal pressures (by 6–10 hPa) for the early part of the year. Relay AWS (Fig. 6.4d) had a record low monthly mean station pressure in June (625.0 hPa) and lower-than-normal pressures for January, July, and September (by 5–7 hPa). By austral spring, the situation had reversed with record high monthly mean station pressure in November now located at Ferrell (990.7 hPa), Marble Point (982.8 hPa), Gill (987.5 hPa; Fig. 6.4f), and Possession Island (985.2 hPa). These records were all 10–11 hPa above the mean. Byrd AWS, Dome C II AWS, and Relay AWS had higher-than-normal pressure for November, and Relay Station set a high monthly mean pressure record in August (638.6 hPa).

On the Ross Ice Shelf, monthly mean wind speeds (not shown) were generally lower than normal except for January and February. Gill had record low monthly mean wind speeds in April (0.5 m s⁻¹), June (1.7 m s⁻¹), and July (2.1 m s⁻¹). Marble Point

sure records set for September, due to an anomalously deep trough extending over the northern Amundsen Sea (Fig. 6.3e). Ferrell, Marble Point, Byrd, and Gill all set record monthly mean low pressures for September (971.8, 965.1, 787.4, and 966.0 hPa, respectively). In addition, Gill AWS recorded a record low monthly mean station pressure in June (972.5 hPa), and Byrd set record lows for monthly mean station pressure in February (803.8 hPa), March (799.1 hPa), June (795.0 hPa), and September (787.4 hPa). Possession Island also had a record low monthly mean station pressure in January (969.7 hPa). While not record setting,

tied the record low for August (2.3 m s⁻¹). Ferrell had a record high monthly mean wind speed for January (7.0 m s⁻¹), and Gill tied its record high monthly mean for February (4.8 m s⁻¹). Gill also reported a record high monthly mean wind speed in September (5.2 m s⁻¹). For the plateau stations, Dome C II had record high monthly mean wind speeds in January and February (4.0 and 3.9 m s⁻¹, respectively), while Relay AWS had a record low monthly mean wind speed in January (5.3 m s⁻¹). Wind speeds at Relay AWS were generally higher than normal for austral spring.

Fig. 6.5. (a) 2016 $P - E$ anomaly (mm); (b) 2015 $P - E$ anomaly (mm). Antarctic regions with > ±30% depar-ture from the reference mean are hatched; sloping denotes negative anomaly and horizontal is positive. (c) 2016 MSLP anomaly (hPa); and (d) 2015 MSLP anomaly (hPa). All anomalies are calculated from the 1981–2010 means. (e) Monthly total $P - E$ (mm; dashed green) for the West Antarctic sector bounded by 75°–90°S, 120°W–180°, along with index trends for EQ-SOI (dashed dark blue, from NOAA CPC) and SAM [dashed light blue, from Marshall (2003)]. Centered annual running means are plotted as solid lines.

### d. Net precipitation (P−E)—D. H. Bromwich and S.-H. Wang

Precipitation minus evaporation/sublimation (P−E) closely approximates the surface mass balance over Antarctica, except for the steep coastal slopes (e.g., Bromwich et al. 2011; Lenaerts and van den Broeke 2012) where wind-driven transport and melt runoff to the ocean can become significant factors. Precipitation variability is the dominant term for P−E changes at regional and larger scales over the Antarctic continent. Precipitation and evaporation fields from the Japanese 55-year reanalysis (JRA-55; Kobayashi et al. 2015) were examined to assess Antarctic net precipitation (P−E) for 2016. JRA-55, the second generation of JRA, has incorporated many improvements relative to its predecessor JRA-25 (Onogi et al. 2007; Bromwich et al. 2007). The JRA-55 result is used here because of these improvements, rather than ERA-Interim used elsewhere, because the JRA-55 result is available with low latency (a few weeks), and so it is available at the time of writing for this annual summary.

Figure 6.5 shows the JRA-55 2016 and 2015 annual anomalies of P−E (Figs. 6.5a,b) and mean sea level pressure (MSLP; Figs. 6.5c,d) departures from the 1981–2010 average. In general, annual P−E anomalies over the high interior of the continent were small (within ±50 mm yr⁻¹), while larger anomalies were observed along the coast, consistent with the low and high snow accumulation in these respective regions. From JRA-55 P−E, higher-than-average net accumulation for 2016 occurred in the southwestern Antarctic Peninsula, eastern Enderby Land and the adjacent Queen Maud Land areas, and Wilkes Land; lower-than-average anomalies were present in the American Highlands, eastern Ross Ice Shelf area, and the northern tip of the Antarctic Peninsula.

These annual P−E anomaly features are generally consistent with the mean annual atmospheric circulation implied by the MSLP anomalies, shown for both 2016 and 2015 (Figs. 6.5c,d; see also Fig. 6.2). In 2016 (Fig. 6.5c), the MSLP anomalies surrounding Antarctica were more regionalized than in 2015 (Fig. 6.5d). The ring of high-pressure anomalies at midlatitudes has diminished. Instead, localized negative anomalies were observed in three Southern Ocean sectors: Atlantic Ocean (between 40°W and 35°E), Indian Ocean (between 105°E and 165°E), and Pacific Ocean (between 160°W and 110°W). The Atlantic Ocean and Indian Ocean negative anomalies had a significant effect on regional net precipitation changes in the coastal areas southeast of those anomaly centers (Fig. 6.5a). Combined with the cyclonic flow associated with the negative anomaly over the South Pacific

(centered on ~135°W; Fig. 6.5c), the strong northerly flow produced high precipitation anomalies over the Bellingshausen Sea and along the west coast of the Antarctic Peninsula in 2016 (Fig. 6.5a). A secondary positive anomaly center located over the Ross Sea (between 170°E and 130°W; Fig. 6.5c) produced stronger offshore flow and less precipitation over the eastern Ross Sea and eastward along the Ross Ice Shelf (Fig. 6.5a).

Earlier studies show that almost half of the moisture transport into interior Antarctica occurs in the West Antarctic sector. Moisture transport has large inter-annual variability associated with variations in ENSO (e.g., Bromwich et al. 2004) and SAM variability (e.g., Fogt et al. 2011). Figure 6.5e shows the time series, with 12-month running means, of monthly total P−E over Marie Byrd Land–Ross Ice Shelf (75°–90°S, 120°W–180°) and the monthly equatorial Southern Oscillation (EQ-SOI) and SAM indices. NOAA Climate Prediction Center EQ-SOI, used here to represent ENSO events, is a standardized sea level pressure difference between the east Pacific (5°N–5°S, 80°–130°W) and the west Pacific–east Indian (5°N–5°S, 90°–140°E) Oceans, and is calculated based on comparatively extensive longitudinal regions centered on the equator. In comparison to the conventional station-based SOI, EQ-SOI is less susceptible to weather noise, and better captures the equatorial trade wind events (see www.climate.gov /news-features/blogs/enso/why-are-there-so-many -enso-indexes-instead-just-one).

It is clear that EQ-SOI and SAM were in phase but had opposite behavior to P−E in most months from 2010 to mid-2011 (Fig. 6.5e). From then on, EQ-SOI and SAM were out of phase through early 2016, especially after mid-2014. Both EQ-SOI and SAM were offsetting factors modulating precipitation, resulting in little overall change of P−E. A positive MSLP anomaly can often be located over the South Pacific (Fig. 6.5c) when SAM is positive and EQ-SOI is negative (Fogt et al. 2011). The weak positive MSLP anomaly in the Ross Sea, with both onshore and offshore flows, has a small net impact on precipitation in this sector. As the seasons progressed from 2015 to 2016, the negative MSLP anomalies over the Ross Sea (Fig. 6.3a) became positive and peaked in 2016 austral spring (Fig. 6.3f). In combination with a weaker ENSO signal, the SAM dominated the behavior of P−E in this region in late 2016.
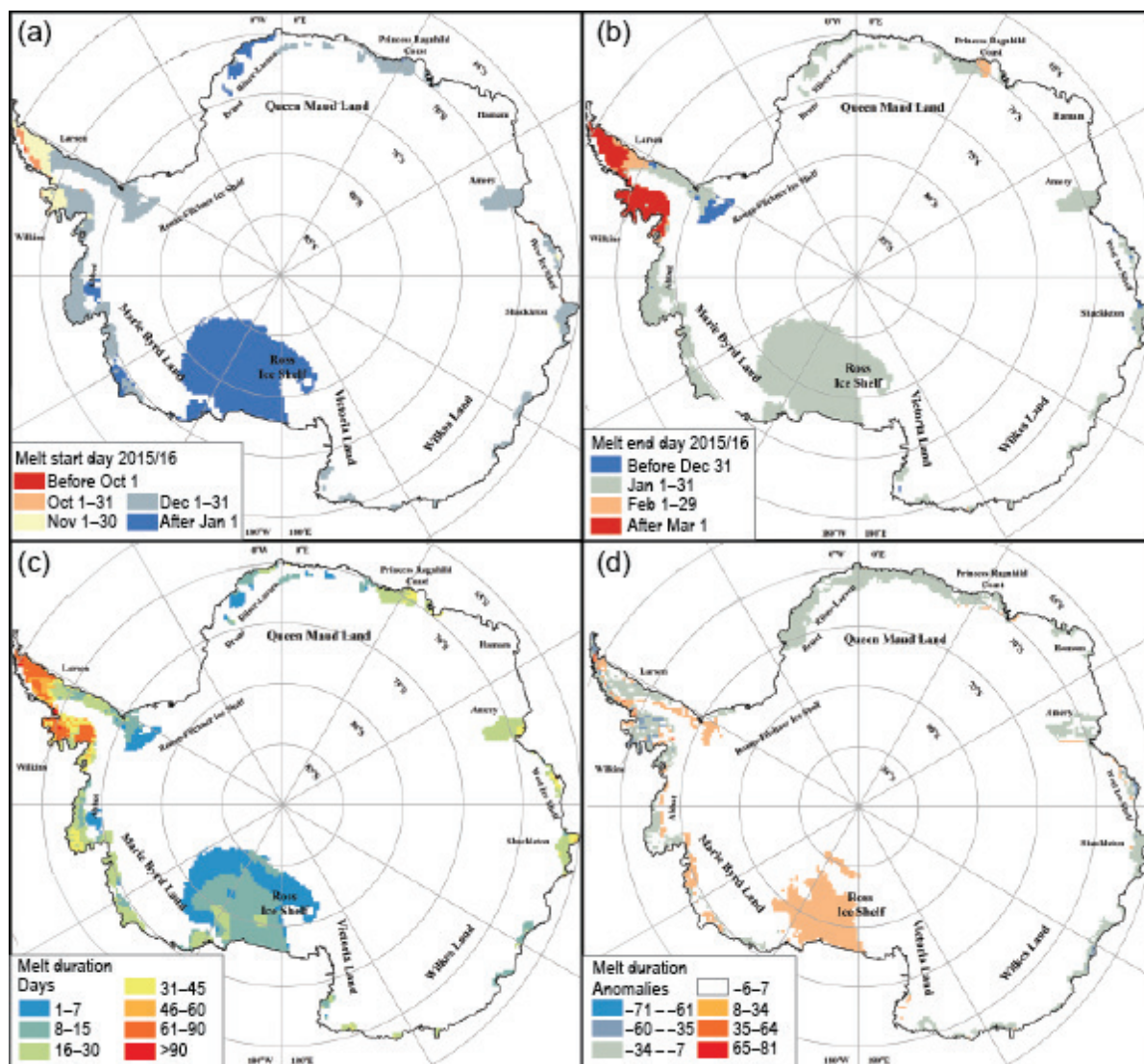
**Fɪɢ. 6.6. Estimated surface melt for the 2015/16 austral summer: (a) melt start day, (b) melt end day, (c) melt duration (in days), and (d) melt duration anomalies (in days).**

*e. Seasonal melt extent and duration*—L. Wang and H. Liu

Surface melt on the Antarctic continent during the 2015/16 austral summer season was estimated from daily passive microwave brightness temperature measurements acquired by the Special Sensor Microwave Imager/Sounder on the Defense Meteorological Satellite Program *F17* satellite. The level-3 Equal-Area Scalable Earth-Grid brightness temperature data were provided by the U.S. National Snow and Ice Data Center (Armstrong et al. 1994). A wavelet transform edge detection method (Liu et al. 2005) was used to delineate each melt event in the time series by tracking its onset and end dates, with the onset day of the first melt event being the start day of the melt season (Fig. 6.6a) and the end day of the last melt event being the end day of the melt season (Fig. 6.6b). The melt duration for each pixel is the total number of melting days during the defined melt season (excluding any refreezing periods that may have occurred between the first and last melt events; Fig. 6.6c). The melt duration anomaly map (Fig. 6.6d) was created by referencing to the mean melt duration computed over the 1981–2010 period (see Fig. 3 in Liu et al. 2006). The melt extent and melt index (Fig. 6.7) are metrics for quantifying the spatiotemporal variability of surface melting (Zwally and Fiegles 1994; Liu et al. 2006). Melt extent (km²) is the total area that experienced surface melt for at least one day, while the melt index (day·km²) is the product of duration and melt extent and describes the total accumulated amount of surface melting.

Figure 6.6c shows the spatial pattern of the melt duration in austral summer 2015/16. The Larsen and Wilkins ice shelves experienced intensive melt sea-
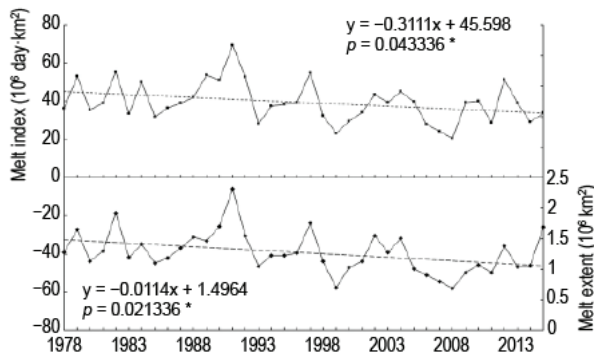
**Fig. 6.7.** Upper panel: Melt index (10⁶ day·km²) from 1978/79 to 2015/16, showing a negative trend (311 100 day·km² yr⁻¹, $p < 0.05\%$). Lower panel: Melt extent (10⁶ km²) from 1978/79 to 2015/16, showing a negative trend (11 400 km² yr⁻¹, $p < 0.05\%$). Year on the x-axis corresponds to the start of the austral summer melt season, e.g., 2008 corresponds to summer 2008/09.

sons of >45 days duration. Areas with moderate melt intensity of 16–45 days duration included the Abbot Ice Shelf, eastern coastal area of Queen Maud Land, and the Amery, West, and Shackleton ice shelves; short-term melt seasons of <16 days duration occurred on the Ross Ice Shelf, the western coastal area of Queen Maud Land, and the Filchner Ice Shelf. The entire eastern Ross Ice Shelf experienced a melt duration ranging from 1 to just over 16 days in the summer of 2015/16, an unusually extensive and long melt season for this region.

Due to the extensive melt occurrence on the Ross Ice Shelf, the overall melt index in 2015/16 showed a slight increase compared to the previous year (Fig. 6.7a), but was still the third lowest in the past seven years. An overall negative trend for the melt index (311 100 day·km² yr⁻¹) since 1978/79 is observed, a statistically significant trend at the 95% confidence level. Nonetheless, melt extent in 2015/16 was the highest since 1998/99 (Fig. 6.7b). Melt extent still exhibits a negative overall trend (−11 400 km² yr⁻¹) since 1978/79, also significant at the 95% confidence level. Negative trends in both melt extent and melt index

are indicated by previous studies as well (Liu et al. 2006; Tedesco 2009; [Tedesco and Monaghan 2009]). The melt anomaly map in Fig. 6.6d shows that the melt season duration in 2015/16 was generally shorter than the historical average, except for the Ross Ice Shelf.

*f. Sea ice extent, concentration, and seasonality—*P. Reid, S. Stammerjohn, R. A. Massom, J. L. Lieser, S. Barreira, and T. Scambos

Both net sea ice extent (SIE) and area (SIA) were close to the 1981–2010 average for January through August 2016, after which there was a dramatic departure from the mean through to the end of the year (Fig. 6.8a). Maximum net SIE peaked on 31 August (18.44 × 10⁶ km²); this was close to the long-term mean daily maximum (18.8 × 10⁶ km²) but was the earliest annual daily maximum SIE on record since consistent satellite records began in 1979. (Prior to 2016, the earliest annual daily maximum SIE was 3 September 1994.) Thereafter, record low monthly mean SIA was recorded from September through December along with record low monthly SIE from October through December. The monthly anomalies
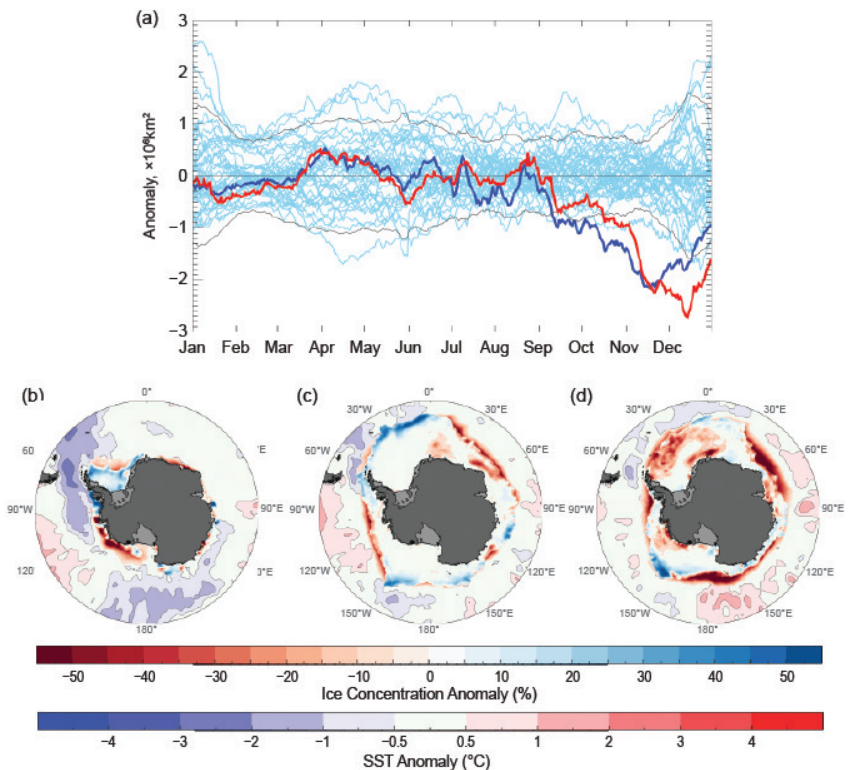


**Fig. 6.8.** (a) 2016 daily anomaly (10⁶ km²) of SH sea ice extent (red line) and area (dark blue line), from the 1981–2010 mean. Thin blue lines represent the historical daily values of extent for 1979–2015, while the thin black lines represents ±2 std. dev. of extent. Sea ice concentration anomaly (%) for (b) Feb (c) Aug 2016 (d) Nov, (relative to 1981–2010 monthly means), along with monthly mean SST anomalies (°C; Reynolds et al. 2002; Smith et al. 2008). Bell is Bellingshausen Sea.

of net SIE and SIA in November 2016 are over 5 standard deviations below the 1981–2010 average. Many individual daily record lows were broken, with 111 (74) days of record low SIA (SIE) between September and December (Fig. 6.8a). These record low values are a considerable departure both from the record high values observed during 2012–14 (Reid and Massom 2015), and also from the small but statistically significant increase in net SIE observed in satellite data since 1979 (Simmonds 2015; Comiso et al. 2017).

Following on from late 2015 (Reid et al. 2016), the first few months of 2016 saw quite distinct large-scale regional variability in the pattern of SIE (Figs. 6.8b, 6.9a). For January–March, very low extent was observed in the Ross and Amundsen Seas (~150°E–110°W) and eastern Weddell Sea–Indian Ocean sector (~0°–60°E), the latter region being nearly ice free along the Antarctic coast from mid-January through early April. In contrast, SIE was particularly high over this period in the Bellingshausen and western Weddell Seas (~110°W–0°), most likely associated with northward Ekman drift due to the contemporary strong westerly winds (Fig. 6.2c) and below-average sea surface temperatures (SSTs; Figs. 6.8b, 6.10b). The contrasting SIE anomaly pattern in the western Weddell–Bellingshausen Seas and western Amundsen/eastern Ross Seas follows on from the anomaly pattern in late 2015, which was influenced by the 2015 El Niño (Reid et al. 2016). In East Antarctica (~60°–150°E), there were locally mixed sea ice anomalies, with higher-than-average SIE being typically coincident with below-average SSTs immediately north of the ice edge (Figs. 6.8b, 6.10b). By the end of March, net SIA and SIE were slightly above the 1981–2010 average (Fig. 6.8a).

The negative SIE anomaly, evident in early April in the Ross Sea, translated over the following few months to a negative SIE anomaly farther to the east, in the Bellingshausen and Amundsen Seas (Fig. 6.9a). Similarly, the positive/negative SIE anomaly in the far western/eastern Weddell Sea migrated eastward over the subsequent several months. This is consistent with the climatological pattern of eastward zonal transport of sea ice anomalies from the strong gyres within the Ross and Weddell Seas and within the Antarctic Circumpolar Current, as shown in Kimura and Wakatsuch (2011), which usually happens from April/May through to about October. From late March–early April, SIE in the eastern Indian Ocean and much of the western Pacific Ocean sectors (~60°–120°E) was anomalously high, partially coinciding with below-average SSTs to the north of the ice edge east of 90°E. The area of anomalously high

SIE in the eastern Indian Ocean migrated eastward into the southwestern Pacific Ocean region over the following months, positioning itself in the vicinity of ~100°–110°E, where it persisted until to about November. By the end of July, net SIE and SIA were both slightly below average (Fig. 6.8a).

During late July and early August, several cyclones passed eastward across the Weddell Sea and into the
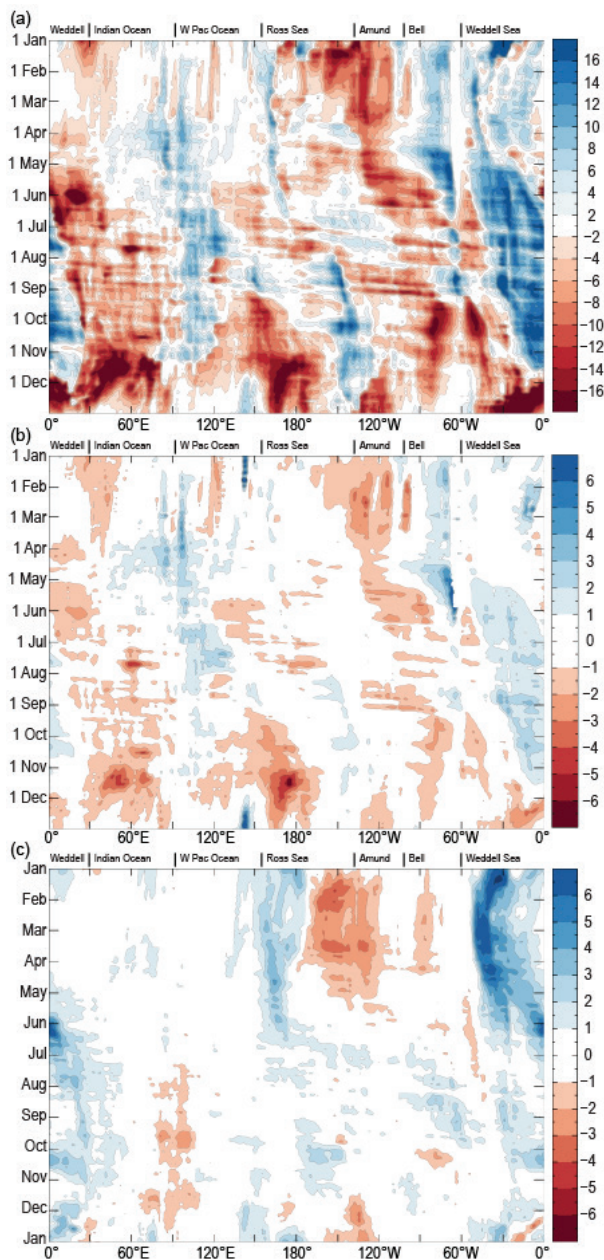


**Fig. 6.9.** Hovmöller plots of (a) daily SH sea ice extent anomalies for 2016 ($\times 10^3$ km² per degree of longitude; from the 1981–2010 mean); (b) standardized sea ice extent; and (c) 1979–2016 trend of sea ice extent ($\times 10^3$ km² decade$^{-1}$). Based on satellite passive–microwave ice concentration data (Cavalieri et al. 1996, updated yearly).
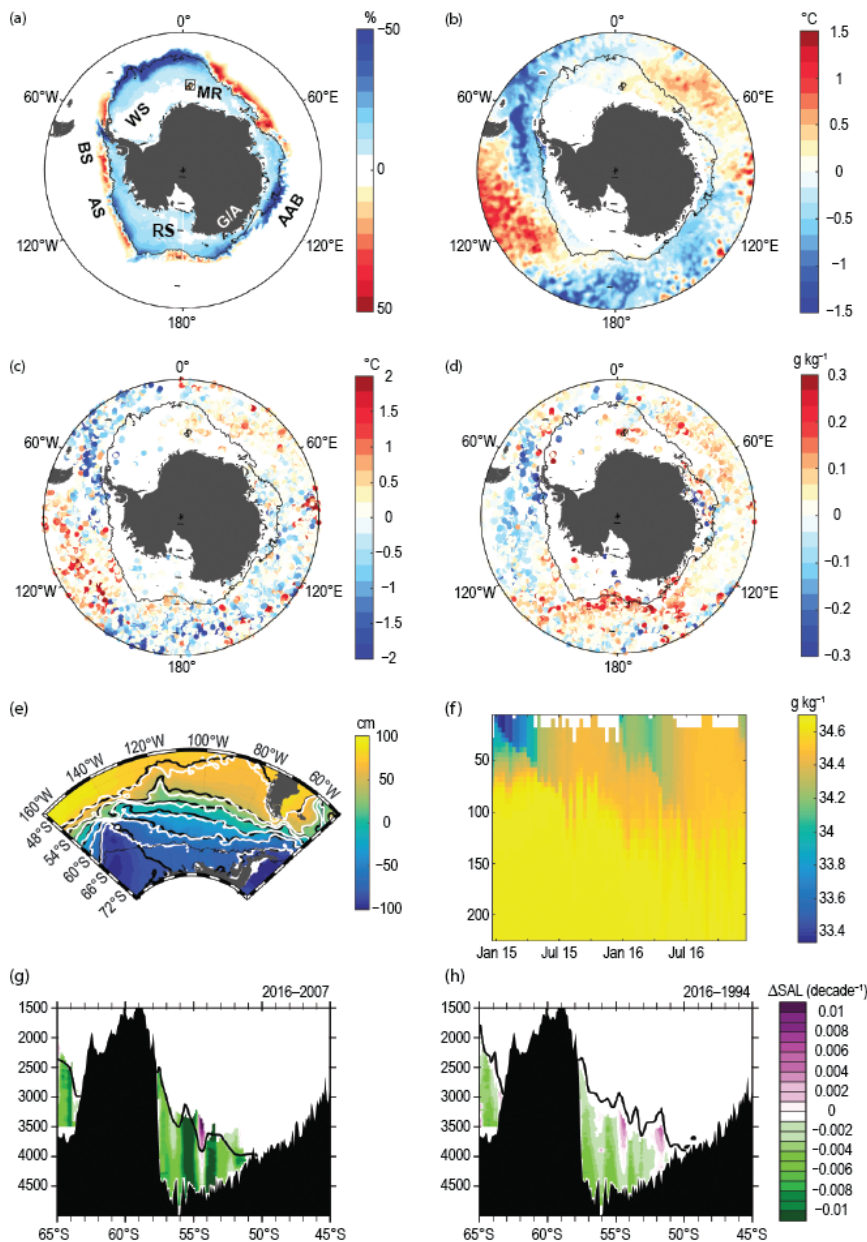
**FIG. 6.10. (a) Sea ice concentration anomaly (%) in Aug 2016 from AMSR-E (Spreen et al. 2008). The gray line in this and subsequent panels is the Aug 2016 80% sea ice concentration contour. Locations discussed in text are denoted: Weddell Sea (WS), Maud Rise (MR), Australian–Antarctic Basin (AAB), George V/Adélie Land Coast (GA), Ross Sea (RS), Amundsen Sea (AS), and Bellinghausen Sea (BS). (b) SST anomaly (°C) for Feb–Jun 2016 (OISST from www.remss.com). (c) Anomaly (°C) from climatological seasonal cycle of mixed layer conservative temperature in Feb–Jun 2016. (d) Same as (c), except for absolute salinity. [For information on the method used for (c) and (d) see Pellichero et al. (2017).] (e) Color and black contours show mean SSH (cm). White contours show mean 2016 SSH after removing SSH linear trend, showing the ACC was displaced poleward in 2016 in this sector. SSH product from Ssalto/Duacs and distributed by Aviso, with support from CNES (www .aviso.altimetry.fr/duacs). (f) Salinity profiles (g kg⁻¹) over Maud Rise from SOCCOM float 9094. (g) Rates of change in PSU of AABW for 2016–2007 for the I08S occupation. (h) Same as (g) but for the change for 2016–1994. The green curve indicates β = 28.27 kg m⁻³ in 2016 (g) and 1994 (h).**

Indian Ocean sector, bringing with them periods of relatively warmer northerly winds to the Queen Maud Land coast. Subsequently, several central-pack polynyas opened up within the eastern Weddell Sea, the first occurring around 5 August (~1800 km²) over Maud Rise (~3°E, 66°S) and lasting for two days. This was followed, from 11 to 29 August, by a larger polynya in the Cosmonaut Sea (~40°–50°E, 66°S). Polynyas are thought to recur in these areas due to a combination of oceanic and atmospheric forcing (e.g., Holland 2000; Beckmann et al. 2001; Arbetter et al. 2004). Analysis within the Southern Ocean section of this chapter (6g) suggests that the Maud Rise polynya in 2016 was probably related to increased deep convection due to the higher-than-average salinity in that region. Above-average SSTs (from the Indian Ocean) may also have contributed by preconditioning the pack ice for polynya formation. Although modest in size compared to the giant polynyas of 1974–76 (Carsey 1980; de Lavergne et al. 2014), the 2016 polynya is significant as it may announce a revival of deep ocean convection in the Weddell Sea. The reemergence implies underlying conditions that may have hastened sea ice retreat (Figs. 6.8c, 6.9a). Over the subsequent two months, sea ice concentration within the Weddell Sea and Indian Ocean sector was predominantly below average.

Similarly, during these few months (August–October), lower-than-average SIC and sea ice coverage was evident within the Ross, Amundsen, and Bellingshausen Seas, apart from a slightly greater extent between ~140°–150°W (Figs. 6.8c, 6.9a). These regions were possibly affected by above-average atmospheric temperatures, as a result of low pressure systems in the East Antarctic and Bellingshausen–Amundsen Seas (e.g., Fig. 6.3e), and SSTs advecting southward within the western and eastern Pacific Ocean (e.g., Fig. 6.8c). SIE in the western Pacific Ocean sector (~100°–120°E) remained slightly higher than average during these months.

By the end of October, large regions showed lower-than-average sea ice concentration, area, and/or extent (Fig. 6.9a), and net SIE and SIA were at record low levels (Fig. 6.8a). From late October through the end of the year, there was a decrease in westerly wind strength around the continent (coincident with the strongly negative SAM index; see Fig. 6.2c) and an influx of warmer water from the north, particularly in the western Pacific Ocean. The reduced westerlies decreased the strength of northward Ekman drift; the influx of warmer water reduced thermodynamic ice growth, respectively. With a thinner sea ice pack at the ice edge, melting occurred earlier in the outer sea ice pack and led to a further reduction in sea ice coverage in the western Ross Sea (~150°E–160°W) and Indian Ocean (~30°–90°E) while compacting the sea ice (increasing its concentration) in the far eastern Weddell (~0°–20°E) and eastern Ross Seas (~170°–130°W). Elsewhere, in the western Pacific Ocean (~90°–150°E) and the Bellingshausen Sea regions (~130°–50°W), SIE was close to average during this period (Fig. 6.9a).

When the daily SIE anomalies are mapped out in space and time, as shown in the Hovmöller plot in Fig. 6.9a, and normalized by their standard deviation (Fig. 6.9b), a few additional outstanding features become clear. Most regions experienced anomalously low SIE for most of the year, with the distinct exception of the Bellingshausen Sea (during the first third of the year), the western Weddell (until December) and the western West Pacific. Notably, the rapid switch from strong positive to strong negative anomalies in the western Weddell Sea in December resulted in 20 daily low records for that area. Similarly, the emergence of strong negative SIE anomalies in the Indian Ocean and western Ross Sea (between 150°E and 180°) sectors from October to December led to 49 and 60 daily record lows, respectively. Another outstanding feature in the standardized figure (Fig. 6.9b) is the positive SIE evident in the summer months in the Mertz

Glacier region (~140°E). This may have resulted from the enhanced westward advection of sea ice across that region within the Antarctic Coastal Current after the breakup of the Mertz Glacier Tongue in 2010 and is also reflected in the trend panel of Fig. 6.9c. In summary, the 2016 regional anomalies stand in distinct contrast to the long-term trends (Fig. 6.9c), with the exception of the negative SIE anomalies in the Amundsen Sea during January–March.

g. *Southern Ocean*—M. R. Mazloff, J.-B. Sallée, V. V. Menezes, A. M. Macdonald, M. P. Meredith, L. Newman, V. Pellichero, F. Roquet, S. Swart, and A. Wåhlin

By connecting the deep ocean reservoir of carbon and heat to the atmosphere, the Southern Ocean is a primary climate regulator. A readily observed component of regulation is the sea ice cover, which provides insulation and affects albedo. As noted in Section 6f, 2016 showed a spectacular decline late in the year, with the lowest ever recorded spring sea ice cover (see Fig. 6.8a). The upper ocean experienced large temperature anomalies consistent with the sea ice patterns discussed in Section 6f (Figs. 6.10b,c). In addition, the open-ocean polynya observed over Maud Rise in August (e.g., see Fig. 6.8c) was likely driven by unusually weak haline stratification (Fig. 6.10f). Observed salinity changes suggest cryospheric influences on multiyear time scales.

1) UPPER OCEAN

From February to June 2016, surface and mixed layer temperatures have a quadrupole structure (Figs. 6.10b,c), similar to sea ice extent anomalies (Fig. 6.10a). A strong positive ENSO event occurred from 2015 into mid-2016. It has been shown that the SST quadrupole pattern is consistent with anomalous heat fluxes associated with strong ENSO events (e.g., Vivier et al. 2010). Indeed, a predicted SST anomaly, derived using a Niño-3.4 SST Index (Rayner et al. 2003) and Southern Ocean SST regression between 2002 and 2015, and the Niño-3.4 index for February to June 2016, explains 27% of the SST anomaly variance between 68° and 60°S, and 13% between 60° and 50°S (not shown).

Sea surface height (SSH) reveals the surface geostrophic circulation and is strongly correlated with SST. In 2016, the Antarctic Circumpolar Current (ACC) appears to have meandered significantly poleward in the Amundsen Sea region (Fig. 6.10e). This may explain the warm SST anomaly and reduced sea ice extent in this region, and it also may imply that relatively warm Circumpolar Deep Water (CDW) was more abundant on the continental shelf and thus more accessible to

the ice shelves at the coast. The 1993–2016 SSH linear trend was removed prior to estimating the 2016 anomaly in an attempt to remove steric trends, but further work is necessary to better partition diabatic warming from adiabatic meandering in interpreting this SSH anomaly.

Mixed layer salinity between February and June 2016 has a clear anomaly pattern (Fig. 6.10d), yet its structure differs from the temperature anomalies (Fig. 6.10c). However, the signal is consistent with sea ice anomalies in late 2015 (Reid et al. 2016) and early 2016 (see Figs. 6.8b, 6.9a), where anomalously low sea ice was observed almost everywhere except in the western Weddell and eastern Bellingshausen Seas (~30°–90°W; Reid et al. 2016). The positive spring–summer sea ice anomaly translates into more freshwater input, in accord with the observed negative salinity anomaly observed that summer–fall in 2016 (Fig. 6.10d). Meanwhile, the largest negative sea ice anomaly in late 2015/early 2016 (e.g., see Figs. 6.8b, 6.9a) was in the western Amundsen and Ross Seas (~90°W–180°), where the largest positive anomaly of salinity was observed in summer–fall 2016.

### 2) The Maud Rise polynya

As noted in Section 6f, an open-ocean polynya was observed over Maud Rise in winter 2016 (see Fig. 6.8c; Fig. 6.10a), likely related to weaker ocean stratification and deeper convection in the region than in previous years. Indeed, floats in the region reveal an anomalously weak halocline in 2016 with respect to earlier observations (Fig. 6.10f). Most austral fall and winter 2016 profiles have weaker stratification than the climatological average, with some profiles showing almost zero stratification in winter (not shown).

It is unclear what caused the weaker haline stratification. The Weddell Sea had anomalously high sea ice extent in austral spring 2015 (Reid et al. 2016). A hypothesis is that increased spring sea ice extent implies more ice being exported from Maud Rise. Increased export leads to either more production and thus more brine rejection in autumn–winter or less ice remaining to provide melt water in spring–summer. Both processes would result in weaker stratification and are also consistent with the apparent deeper mixing beginning in spring 2015 (Fig. 6.10f).

### 3) Deep ocean

Observations of most of the deep Southern Ocean are not made annually. The 2015 report (Sallée et al. 2016) assessed 140°E between 1969 and 2015, revealing a significant long-term freshening trend of approximately −0.01 PSU decade⁻¹. This section crosses the eastern side of the Australian–Antarctic Basin (AAB), and Antarctic Bottom Water (AABW) found in the AAB is sourced from the George V/Adélie Land coast (GA; 136°–154°E) and the Ross Sea. In 2016, the I08S (95°E) line was occupied. (IO8S is a World Ocean Circulation Experiment Hydrographic Program indicator.) This line, which was also occupied in 1994 and 2007 (e.g., Figs. 6.10g,h), crosses the western side of the AAB and is also influenced by the GA and Ross Sea AABW source regions. As reported in Menezes et al. (2017), the I08S data showed AABW was warmer and less dense, with changes of $0.06 \pm 0.01°C$ decade⁻¹ and $0.011 \pm 0.002$ kg m⁻³ decade⁻¹ (e.g., Fig. 6.10h), respectively. A freshening was observed, with mean rates of $-0.002 \pm 0.001$ g kg⁻¹ decade⁻¹ for the period 1994 to 2007 and $-0.006 \pm 0.002$ g kg⁻¹ decade⁻¹ for 2007–16 (e.g., Fig. 6.10g). The results at 95°E (Figs. 6.10g,h) and 140°E (Sallée et al. 2016) support the hypothesis that increased freshwater input from the ice sheet, either through runoff, basal melting, or iceberg contribution, is contributing to a deep Southern Ocean freshening trend. Changes to sea ice transport and spatial changes in high-salinity shelf water input may also be factors in this trend.

### 4) Observational gaps and future outlook

Significant gaps exist in the observations needed to assess the state of the Southern Ocean climate. As in previous years, this report focuses on physical rather than biogeochemical observations, due to a paucity of the latter. However, coverage is improving. Two new projects aim to increase knowledge of the Southern Ocean carbon cycle, giving promise that future reports will address this fundamental component of the climate system. See Sidebar 6.1 on the ORCHESTRA and SOCCOM programs for more information on these efforts. ORCHESTRA and SOCCOM, along with other efforts such as the consortium that is instrumenting marine mammals (www.meop.net/), are also contributing much-needed observations within the seasonally sea ice covered areas. However, other significant gaps remain, including the ocean below perennial sea ice covered areas and ice shelves, the relatively shallow continental shelf seas, and the ocean deeper than 2000 m (Schofield et al. 2016).

Climate change is one of the most pressing issues facing humanity and life on Earth. The role of the oceans in governing the rate of climatic change is now clear, with more than 90% of the extra heat and approximately one-third of the extra carbon emitted since the Industrial Revolution having been absorbed by the ocean (Khatiwala et al. 2013; Rhein et al. 2013). However, not all oceans contribute equally—the Southern Ocean is disproportionately influential due to its unique pattern of circulation and the physical and biogeochemical processes that it hosts (e.g., Marinov et al. 2006; Marshall and Speer 2012).

Unfortunately, the Southern Ocean is also one of the most poorly measured regions of our planet. Its remoteness and inhospitable nature—especially in winter, when much of the surface is covered by sea ice—has led to it being the world's largest data desert. This has slowed progress in understanding the key processes that give it such strong climatic importance, with the consequence that their representation in ocean and climate models remains inadequate.

Two new programs have been initiated with the aim of improving our knowledge of the Southern Ocean. ORCHESTRA—Ocean Regulation of Climate via Heat and Carbon Sequestration and Transports (www .orchestra.ac.uk; Fig. SB6.I)—is a collaboration of seven UK research institutes. Over the next five years, it will conduct a sequence of hydrographic/tracer/carbon research cruises that will quantify the storage and transports of heat and carbon into and through the Atlantic sector of the Southern Ocean, and that will contribute to the international GO-SHIP program. Autonomous systems for air–sea carbon fluxes will also be developed and deployed, and innovative technology (including the tagging of marine mammals with oceanographic instruments) will be used to gather data year-round. Dedicated flights with the British Antarctic Survey's meteorological aircraft (MASIN) will be coordinated with the in situ ocean data collection, including missions over different sea states and sea ice conditions.

Contemporaneously, the Southern Ocean Carbon and Climate Observations and Modeling (SOCCOM; soccom .princeton.edu; Fig. SB6.2) program will deploy ~200 automated profiling floats throughout the Southern Ocean, with biogeochemical sensors measuring nitrate, oxygen, and pH as well as chlorophyll fluorescence and particle backscatter. The SOCCOM consortium includes eight academic and private research institutions and close collaborations with NOAA laboratories. More than 60 SOCCOM profiling floats
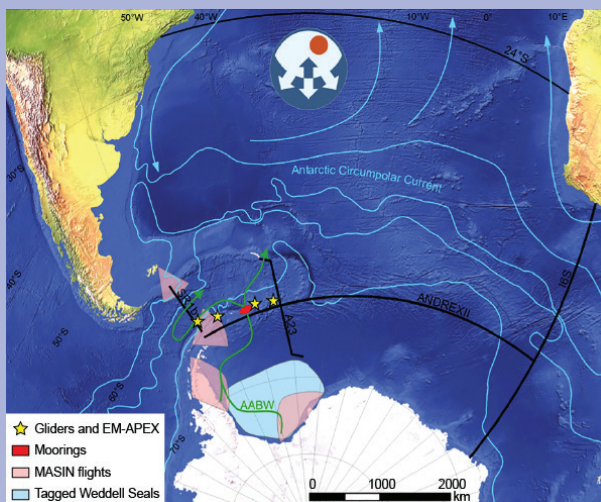


**FIG. SB6.I. Schematic of ORCHESTRA fieldwork in the Atlantic region of the Southern Ocean. Black lines denote major hydrographic/carbon sections undertaken by ship. Pink sectors denote missions with the BAS MASIN meteorological aircraft. The light blue denotes the region of ocean data recovery from tagged Weddell seals. The ORCHESTRA deep mooring cluster is marked in red, and nominal deployment positions for ocean gliders and autonomous profiling explorer (EM-APEX) floats are marked in yellow. Profiling float data from the Argo and SOCCOM networks are available throughout the region.**

are already in the ocean reporting data every 10 days from all regions of the Southern Ocean, including under sea ice, with some records now approaching three years in length (Fig. SB6.2). These floats will be used to constrain regional and annual estimates of Southern Ocean acidification and uptake of carbon dioxide, as well as the cycling of nutrients and oxygen including the biological pump strength, phytoplankton ecology and productivity, the position of major biogeochemical fronts, and the transport across fronts. SOCCOM will operate through the year 2020, and all float data are being made publicly available in near-real time.

Both programs will use the in situ data collected to improve the high-resolution models used to simulate the Southern Ocean. ORCHESTRA will develop new schemes within the NEMO model (www.nemo-ocean.eu) including a hybrid coordinate system to better simulate the descent of dense water into the ocean depths. The data from the SOCCOM floats will be used to constrain a biogeochemical version of the Southern

Ocean state estimate model (SOSE; Mazloff et al. 2010) to provide a comprehensive assessment of the contemporaneous carbon cycle. The SOSE output will then be used to improve projections of future carbon cycle using a coupled Earth system model. These improvements will be taken up by the climate modeling centers in both countries, with output made available to the Southern Ocean Model Intercomparison Project and IPCC.

This combination of programs will leave a lasting legacy that will guide the future of research on this globally important topic. The datasets gathered will constitute benchmarks for the Southern Ocean's role in capturing anthropogenic carbon and heat from the atmosphere and will have value in perpetuity. The improved mechanistic understanding of key processes will be incorporated into the coupled models used for climate predictions, upon which advice to policy makers is ultimately based.
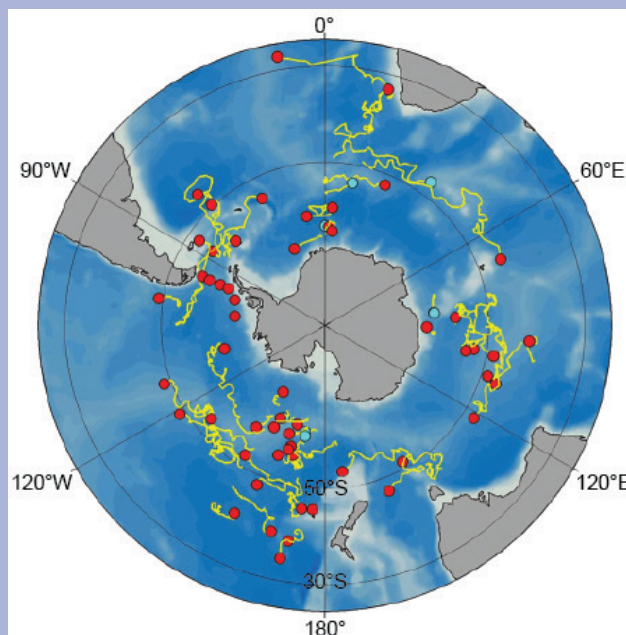


FIG. SB6.2. Locations of the 64 current **SOCCOM** floats **as of 31 Dec 2016. Red dots indicate operating floats while blue dots are inoperative floats. Yellow lines indicate trajectories of floats since deployment. Approximately 200 SOCCOM floats will be deployed in the Southern Ocean by 2020.**

*h. 2016 Antarctic ozone hole*—P. A. Newman, E. R. Nash, S. E. Strahan, N. Kramarova, C. S. Long, M. C. Pitts, B. Johnson, M. L. Santee, I. Petropavlovskikh, and G. O. Braathen

The Antarctic ozone hole is a severe ozone depletion that regularly appears in austral spring. In 2016, Antarctic stratospheric ozone depletion was less severe compared to the 1991–2006 average (a period of peak chlorine and bromine over Antarctica), but ozone levels were still low compared to pre-1990 levels. Figure 6.11a displays the ozone column between 12 and 20 km derived from NOAA South Pole balloon profiles averaged over 21 September to 16 October (the period with the largest ozone depletion). The 2016 South Pole ozone column was ~6 Dobson units (DU) higher than the 1991–2006 average (horizontal dashed line in the figure), and all ozone column means through the ozone minimum seasons since 2009 have been higher than this 1991–2006 average.

Satellite column observations over Antarctica (*Aura* OMI sensor) also suggest relatively weaker-than-average ozone depletion. Figure 6.11b shows the average of daily minimum total column ozone values over the 21 September to 16 October period. The 2016 total column (Fig. 6.11b) of 124 DU is ~13 DU higher than the 1991–2006 average (horizontal dashed line), consistent with the South Pole partial column (Fig. 6.11a). Since 1991, there have been only five ozone holes with larger minimum values than those in 2016. The 2016 ozone hole area was 20.9 million km$^2$ (averaged from the 7 September–13 October daily estimates); only five ozone holes have had a smaller area.

Both the temperature and chlorine levels of the Antarctic lower stratosphere control the ozone hole's severity. Figure 6.11c displays the time series of 50-hPa September mean temperatures (K) in the 60°–90°S region from the NASA MERRA-2 (black points) and from the ECMWF ERA-Interim (red points) reanalyses. Note that the ERA-Interim values are biased low with respect to the MERRA-2 data for the period up to 1998, but the two datasets are in excellent agreement from 1999 to the present. The figure

(a) South Pole 12–20 km column

(b) Antarctic Sep minimums avg.

(c) 60°–90°S 50-hPa

ERA-i
MERRA-2
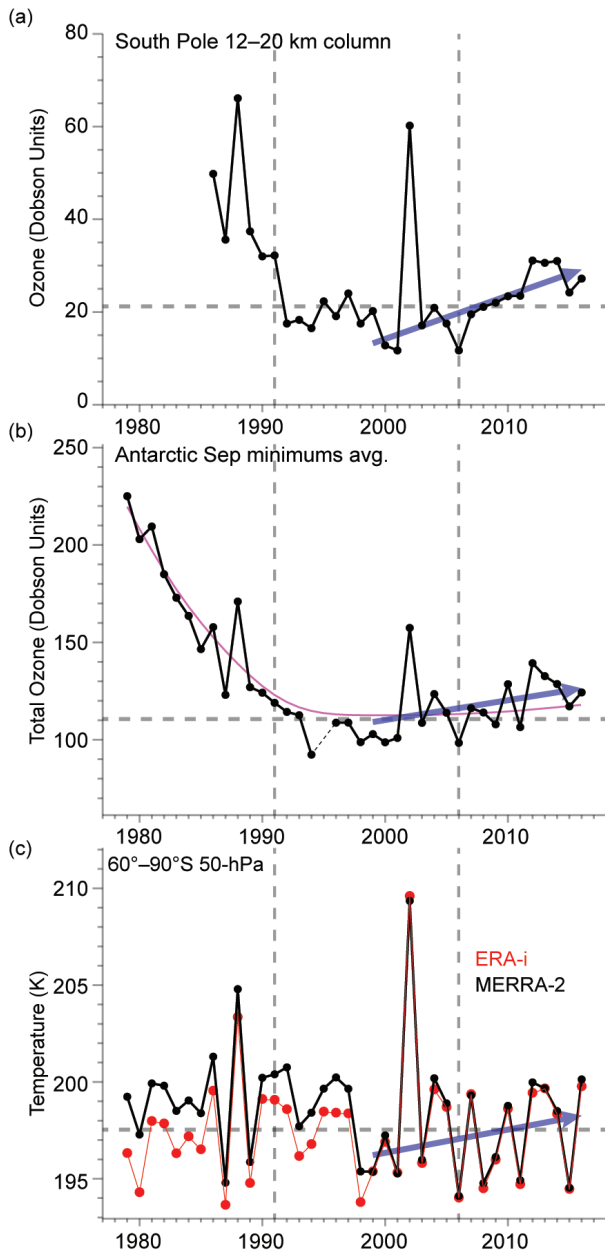
**Fig. 6.11. (a) Column ozone (DU) measured within the primary depletion layer (12–20 km) by NOAA South Pole ozonesondes 21 Sep–16 Oct 2016. (b) Satellite daily total ozone minimum values (DU) averaged over 21 Sep–16 Oct. (c) 50-hPa Sep temperature (K) averaged over 60°–90°S for MERRA-2 (black points) and ERA-Interim (red points). Blue lines indicate 1999–2016 trend; dashed lines indicate 1991–2006 average values. The magenta curve in (b) is the quadratic fit of total ozone to EESC.**

shows that the 2016 average temperature was a couple of degrees higher than the average over 1991–2006, the peak ozone hole period.

The 2016 stratospheric dynamical conditions were slightly more active than the 1980–2015 average. The 100-hPa eddy heat flux is a metric of both wave propagation into the stratosphere and the strength of the downward motion over Antarctica. In 2016 the magnitude of the 100-hPa eddy heat flux was above average for the August–September period (not shown). Consequently, the Antarctic stratospheric vortex was warmer than average (Fig. 6.11c) and its jet flow was slightly weaker than average (not shown).

The 2016 ozone hole broke up around 24 November (fifth earliest since 1980), approximately two weeks earlier than the average break-up date for the last 20 years (2015 break-up was 21 December). The "break-up" is estimated when total ozone values less than 220 DU disappear. The ozone hole break-up is tightly correlated with the lower stratospheric polar vortex break-up, which is driven by late spring wave events propagating upward into the stratosphere. The earlier break-up date in 2016 was due to stronger wave activity in October and November that enabled the mixing of ozone-rich midlatitude air into the polar midstratosphere.

The slightly higher 2016 Antarctic lower stratospheric temperature likely lessened the severity of the 2016 ozone hole. Figure 6.12 displays the ozone anomalies associated with the lower stratospheric temperatures from ERA-Interim (Fig. 6.11c).
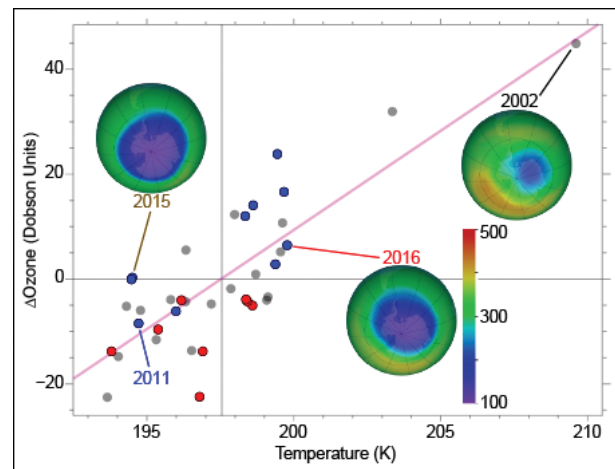


**Fig. 6.12. Column ozone anomalies (DU) versus ERA-Interim 50-hPa Sep mean temperatures (K) in the 60°–90°S region (see Fig. 6.11c). The inset images are total column ozone averages over 21 Sep–16 Oct periods. Red points indicate years 1992–2000 (large ozone holes); blue points represent the last decade, 2007–16. The vertical line is the temperature average for the entire period. The magenta line shows the linear fit.**

These ozone anomalies are calculated by fitting effective equivalent stratospheric chlorine (EESC, an estimator of human-produced chlorine and bromine loading of the stratosphere) with a 5.2-year mean age to the total ozone (fit is shown as the magenta line in Fig. 6.11b). The ozone anomalies from this EESC fit are well correlated with temperature anomalies. The above-average column ozone in 2016 was likely the result of above-average temperatures, with a small contribution from decreasing EESC.

Satellite observations of chlorine and ozone in the 2016 Antarctic lower stratosphere were not exceptionally different from those in the last 10 years. *Aura* satellite Microwave Limb Sounder (MLS) observations of hydrogen chloride (HCl: Fig. 6.13a), chlorine monoxide (ClO: Fig. 6.13b), and ozone (Fig. 6.13c) are shown for the Antarctic polar vortex. The reaction of HCl with chlorine nitrate (ClONO$_2$) on the surfaces of polar stratospheric cloud (PSC) particles forms chlorine gas (Cl$_2$) and causes HCl to decline during the June–July period (Fig. 6.13a). Cl$_2$ is easily photolyzed by visible light, and the ozone-reactive ClO steadily increases as the sun returns to Antarctica (Fig. 6.13b). Chlorine (Figs. 6.13a,b) and ozone (Fig. 6.13c) in the 2016 Antarctic stratosphere (red) were within the 2004–15 climatology (gray).

PSCs provide particle surfaces that enable heterogeneous chemical reactions to release chlorine for catalytic ozone loss. Temperatures provide a useful proxy for PSCs, but the *Cloud-Aerosol Lidar and Infrared Pathfinder Satellite Observation (CALIPSO)* satellite provides direct observations. Figure 6.13d displays the 2016 PSC volume (red line). High levels of PSCs started later than usual in 2016 and reached very large volumes in midwinter. However, these midwinter values had minimal impact on ozone because depletion requires sunlight. The 2016 PSC volumes during the key depletion month of September were some of the lowest in the record.

The 2016 observations continue to add to our confidence that Antarctic ozone levels are increasing, as noted in Newman et al. (2015), Nash et al. (2016), and Solomon et al. (2016). The South Pole 1999–2016 stratospheric ozone trend of 0.94 DU yr$^{-1}$ (Fig. 6.11a, blue line) is statistically significant (99% confidence) if 2002, a year of sudden major warming in the stratosphere, is excluded from the trend, and not significant, at 0.44 DU yr$^{-1}$, if 2002 is included. Similarly, the satellite daily total ozone minimum values trend (Fig. 6.11b, blue line) is 1.6 DU yr$^{-1}$ (99% confidence without 2002), and 1.0 DU yr$^{-1}$ if 2002 is included (not significant). The EESC fit to ozone is shown in Fig. 6.11b as the magenta line. Because of
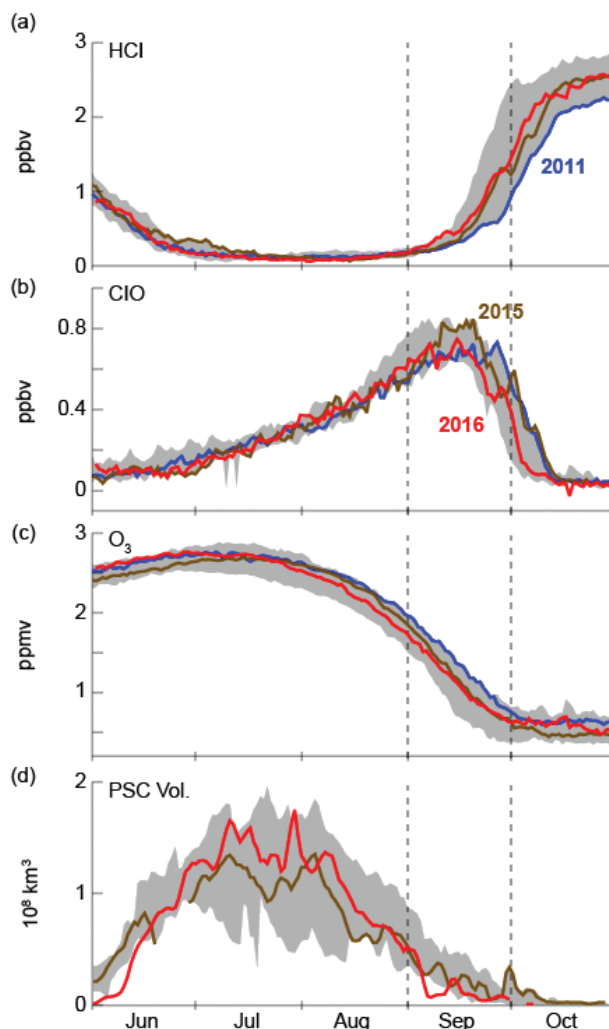


**Fig. 6.13. Antarctic 2016 vortex-averaged concentrations (red lines) of: (a) HCl (ppbv), (b) ClO (ppbv), and (c) ozone (ppmv) from *Aura* MLS (updated from Manney et al. 2011). The MLS averages are made inside the polar vortex on the 440-K potential temperature surface (~19 km or 60 hPa). Gray shading shows the range of daily Antarctic values for 2004–15, and 2011 is blue line while 2015 is brown. (d) *CALIPSO* PSC volume (× 10$^8$ km$^{-3}$; updated from Pitts et al. 2009). Gray shading in (d) is for 2006–15.**

the slow decline of chlorine and bromine in the atmosphere, the Antarctic ozone upward trend expected from EESC is relatively small (5–6 DU between 1999 and 2016) and considerably less than the one-sigma interannual residual variability of 14 DU.

The Antarctic lower stratospheric temperature trend is weakly positive during the key September period for ozone depletion. From Fig. 6.11c, the trend is 0.12 K yr$^{-1}$ (90% confidence without 2002), and −0.025 K yr$^{-1}$ if 2002 is included (not significant). While ozone anomalies are highly correlated with temperature (r = 0.82 in Fig. 6.12, statistically

significant at >99.9% confidence level), the 2007–16 ozone anomalies are higher than expected (Fig. 6.12, blue points), while the 1992–2000 ozone anomalies are lower than expected (Fig. 6.12, red points). This is consistent with EESC levels declining since 2000; however, the fact that the ozone trends are larger than the temperature trends suggests that additional processes (e.g., long-term transport, spring initial conditions for ozone) are also playing a role in the ozone trend.

Attribution of ozone hole improvement to declining EESC levels is still difficult. A mean age of 5.2 years is used to estimate EESC (Strahan et al. 2014). Since the 2000–02 peak of 3.79 ppb, EESC has decreased to an estimated 3.43 ppb (a drop of 10%). This is a 22% drop towards the 1980 level of 2.05 ppb, a year in the "pre-ozone hole" period. *Aura* MLS nitrous oxide ($N_2O$) measurements have been used to estimate Antarctic stratospheric inorganic chlorine ($Cl_y$) levels (Strahan et al. 2014) and quantify their transport-driven interannual variability. This transport variability, driven by the direction of the tropical zonal wind (i.e., the quasi-biennial oscillation), has resulted in Antarctic stratospheric $Cl_y$ levels in 2014, 2015, and 2016 that were higher than in previous years (e.g., 2011–13) and similar to levels found prior to 2010.

Further information on the ozone hole with data from satellites and ground and balloon instruments, can be found in the *WMO Antarctic Ozone Bulletins* (www.wmo.int/pages/prog/arep/gaw/ozone/index .html).